

Crystal structure, stability, spectroscopy, electronic structure, and ultrafast excited-state dynamics of the elusive iron(II) phthalocyanine axially coordinated with DABCO ligands

Dustin E. Nevonen^a, Jacob Schaffner^b, Paul Hanrahan^b, Michael Shepit^c, Johan van Lierop^c, David A. Blank*,^b and Victor N. Nemykin*,^{◊,a}

Received 24 December 2022 Accepted 17 February 2023

Dedicated to Prof. Jonathan L. Sessler on the occasion of his 65th birthday

ABSTRACT: The elusive PcFe(DABCO)₂ (Pc = phthalocyaninato(2-) ligand; DABCO = 1,4-diazabicyclo[2.2.2]octane) complex was prepared and characterized by UV-Vis, MCD, ¹H NMR, and Mössbauer spectroscopies. The X-ray crystal structure of this complex indicates the longest Fe-N(DABCO) bond distance among all known PcFeL₂ complexes with nitrogen donors as the axial ligands. The target compound is only stable in the presence of large access of the axial ligand and rapidly converts into the (PcFe)₂O μ-oxo dimer even at a modest temperature. The electronic structure of the PcFe(DABCO)₂ complex was elucidated by DFT and TDDFT methods. The DFT calculations predicted a very small singlet-triplet gap in this compound. The femtosecond transient absorption spectroscopy is indicative of extremely fast (~200 fs) deactivation of the first excited state in PcFe(DABCO)₂ with a lack of formation of the long-lived low-energy triplet state.

KEYWORDS: iron phthalocyanine, DABCO, X-ray crystallography, MCD, DFT, transient absorption spectroscopy.

INTRODUCTION

Because of its very rich coordination chemistry that spans between several oxidation and spin states, iron phthalocyanine attracted a lot of attention [1–6]. For instance, monomeric and dimeric iron phthalocyanine derivatives were used in C-H bond activation reactions [7–18], as analytical sensors [19–23], and active components of electrocatalytic reactions [24–26]. Bis-axially coordinated diamagnetic low-spin iron(II) PcFeL₂, PcFeL'L", and [PcFeX₂]²⁻ complexes (L is neutral and X is anionic ligands) have been known for at least a half-century [27–35]. PcFeL₂ complexes with axial nitrogen

donors have been extensively studied by UV-Vis, MCD, and Mössbauer spectroscopies, while many of their molecular structures were elucidated by X-ray crystallography [36-43]. It was shown that the axial coordination of nitrogen donors is very sensitive to the steric properties of the axial ligand. In particular, 2-substituted pyridines, sterically crowded azoles, and tertiary amines cannot coordinate with iron(II) phthalocyanine. One interesting exception to this trend was reported by Hanack and co-workers who were able to synthesize monomeric PcFe(DABCO)₂ and polymeric [PcFe(DABCO)] complexes (DABCO = 1,4-diazabicyclo[2.2.2]octane) in which the sterically strained tertiary DABCO amine was able to axially coordinate to iron(II) phthalocyanine (Scheme 1).44 The monomeric PcFe(DABCO), and polymeric [PcFe(DABCO)]_n complexes were characterized by Mössbauer spectroscopy, solution and/or solid-state

^aDepartment of Chemistry, University of Tennessee, Knoxville, TN 37996, USA

^bDepartment of Chemistry, University of Minnesota, Minneapolis, MN 55455, USA

^cDepartment of Physics and Astronomy, University of Manitoba, R3T 2N2 Winnipeg, MB, Canada

^oSPP full member in good standing.

^{*}Correspondence to: Victor Nemykin, e-mail: vnemykin@utk.

UV-Vis spectroscopy, and conductivity measurements [44, 45]. The quadrupole splitting for these compounds at room temperature is larger than that in the parent PcFe(II) complex, which, taking into consideration recent discussions in the field, implies a very long Fe-N(DABCO) bond distance. Such a bond elongation, in turn, should significantly reduce the singlet-triplet gap in the PcFe(DABCO)₂ complex, thus making this compound a potential candidate for singlet-triplet fission chemistry and singlet-triplet spin crossover processes. In order to probe this hypothesis, we have synthesized the PcFe(DABCO)₂ complex and probed its electronic structure by an array of steady-state and time-resolved spectroscopic methods, X-ray crystallography, and theoretical calculations.

RESULTS AND DISCUSSION

Hanack and Scheider prepared the PcFe(DABCO)₂ complex by melting a large excess of the DABCO ligand over PcFe in a sealed glass tube for 6 h at 170–175°C [44]. In our hands, the constant sublimation of the DABCO ligand created some problems. Thus, we used a microwave reactor and sealed tube to conduct the synthesis of the target compound. This method allowed for the preparation of the PcFe(DABCO)₂ compound in 15 minutes. Taking into consideration the low thermal stability of the PcFe(DABCO)₂ complex, we sublimed the excess of DABCO ligand off of the final product in a high vacuum at room temperature (Scheme1). The dark green sample obtained in this way has a satisfactory elemental analysis result and contains one water molecule (similar to Hanack's report) and half of a DABCO molecule (consistent with the X-ray crystallography discussed below) per phthalocyanine. However, once dissolved in an organic solvent, it quickly transforms into the (PcFe)₂O μ-oxo dimer [46] even at room temperature. Thus, in order to collect spectroscopic data on the PcFe(DABCO)₂ complex, we used a lightly colored sample of this compound obtained directly from synthesis without sublimation of

PcFe
$$\xrightarrow{+L}$$
 PcFeL₂

N $\stackrel{\downarrow}{L}$ N $\stackrel{\downarrow}{L}$ PcFeL₂

L[PcFeL]_n $\stackrel{\downarrow}{-L}$ PcFeL

PcFeL

L[PcFeL]_n $\stackrel{\downarrow}{-L}$ PcFeL

L[PcFe]₂O $\stackrel{\downarrow}{-L}$ (PcFe)₂O

DABCO QUIN

Scheme 1. Preparation and transformation of the PcFe(DABCO)₂ complex.

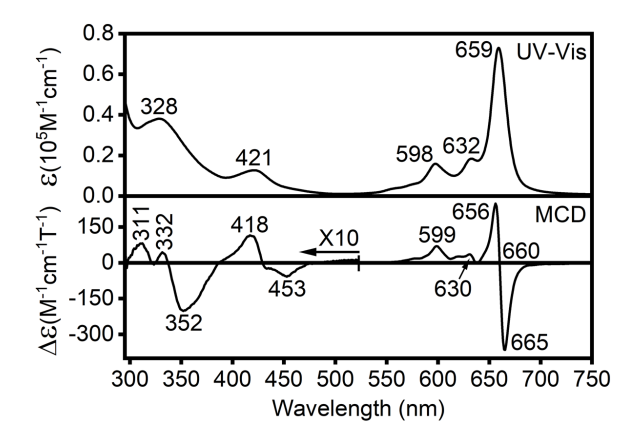


Fig. 1. UV-Vis and MCD spectra of the PcFe(DABCO)₂ complex in o-DCB.

the excess DABCO ligand. This sample is stable in solution for a prolonged time as long as no heat is applied to it. We also attempted to prepare the sterically strained PcFe(QUIN)₂ complex (QUIN = 1-azabicyclo[2.2.2]-octane or quinuclidine). However, in this case, we were unable to isolate the pure target compound, which is again, indicative of the high sensitivity of PcFe to the steric properties of the axial ligand since the cone angle of DABCO is expected to be smaller than that of QUIN.

As mentioned above, in our hands, the PcFe(DABCO)₂ complex was only stable in the presence of a large excess of the axial DABCO ligand. In this case, the UV-Vis and MCD spectra of PcFe(DABCO), (Fig. 1) are very similar to those observed for the PcFeL2 complexes axially coordinated to aliphatic amines [41–43]. On the contrary, when an excess of the DABCO ligand was sublimed at 50°C, the UV-vis spectrum of this much darker sample indicates the formation of μ -oxo dimer in solution (Fig. 1).⁴⁶ Even when a solution of the PcFe(DABCO)₂ sample in o-dichlorobenzene (o-DCB/DABCO system) was heated stepwise inside of a standard (l = 1 cm) UV-Vis cuvette, its transformation into the u-oxo dimer can be seen even at 30 °C (Fig. 2). Following the discussion of Hanack and co-workers on the formation of the polymeric (DABCO) [PcFe(DABCO)]_n species [44], we speculate that the initial

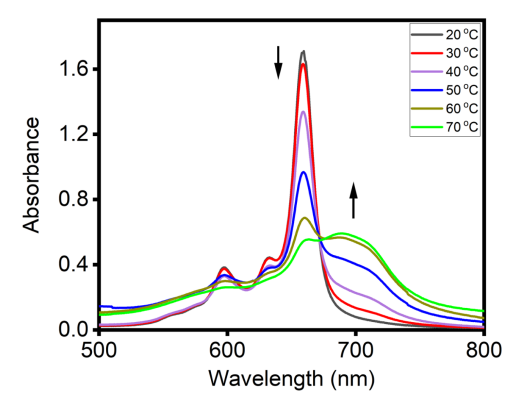


Fig. 2. Transformation of the $PcFe(DABCO)_2$ complex to $(PcFe)_2O$ dimer as a function of temperature in o-DCB.

PcFe(DABCO)₂ complex, even upon mild heating, loses one of the axial ligands and then either forms oligomeric subunits of the general formula (DABCO)[PcFe(DABCO)] $_n$ or an axially coordinated μ -oxo [(DABCO)PcFe]₂O dimer that transforms into the (PcFe)₂O complex (Scheme 1).

The UV-Vis spectrum of PcFe(DABCO), is dominated by the Q-band (typical for this class of compounds) [41–43] observed at 659 nm with two vibronic satellites at higher energies observed at 632 and 598 nm. The MLCT band was observed at 421 nm, and the Soret band at 328 nm. The MCD spectrum of PcFe(DABCO)₂ in the O-band region is dominated by a very strong A-term centered at 660 nm and two B-terms of positive amplitude are observed at 630 and 599 nm. The MCD spectrum in the MLCT region is consistent with the data reported by Stillman and our groups for similar compounds [41–43]. It reflects the presence of two closely spaced A-terms that are dominated by d_{π} (Fe) $\rightarrow b_{1\mu}$ (Pc, π^*) and d_{π} (Fe) \rightarrow b₂₀ (Pc, π^*) single-electron transitions. The Soret band correlates well with the MCD A-term centered at 337 nm. The UV-Vis spectra of the pre-heated sample or the sample exposed to laser radiation discussed in the time-resolved spectroscopy section have a clear shoulder in the 680-730 nm region as well as increased intensity of the band observed at 627 nm. The MCD spectrum of such a sample in the 680-730 nm range resembles that of the µ-oxo dimer compound, thus confirming this complex formation (Fig. 3). Growth of the band at 627 nm might be associated with the formation of the [(DABCO)-PcFe₂O complex (see discussion below).

The Mössbauer spectra of the $PcFe(DABCO)_2$ complex were measured at room temperature and 20 K (Fig. 4). At both temperatures, a single doublet with parameters listed in Table 1 was observed. Since this quadrupole splitting is larger than in the parent PcFe(II) complex and significantly larger than in $PcFeL_2$ complexes with axial primary and secondary amines (Table 1), one might expect that the $Fe-N_{axial}$ bond distance in the $PcFe(DABCO)_2$ complex will exhibit the following trend: $PcFe(NH_2R)_2 < PcFe(NHR_2)_2 < PcFe(DABCO)_2$. To prove this hypothesis, we grew a single crystal of the

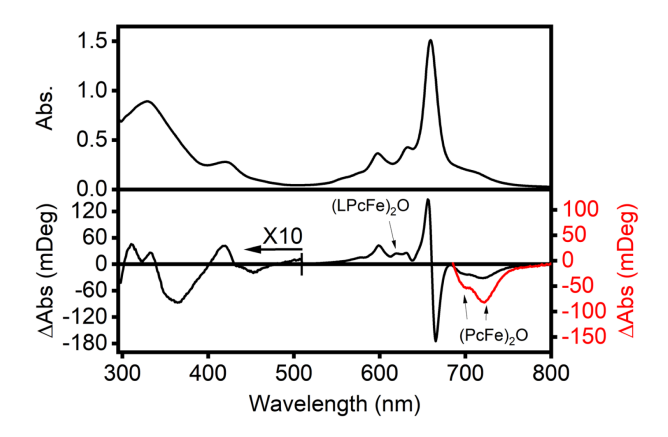


Fig. 3. UV-Vis and MCD spectra of the PcFe(DABCO)₂ complex pre-heated at 30 °C in o-DCB.

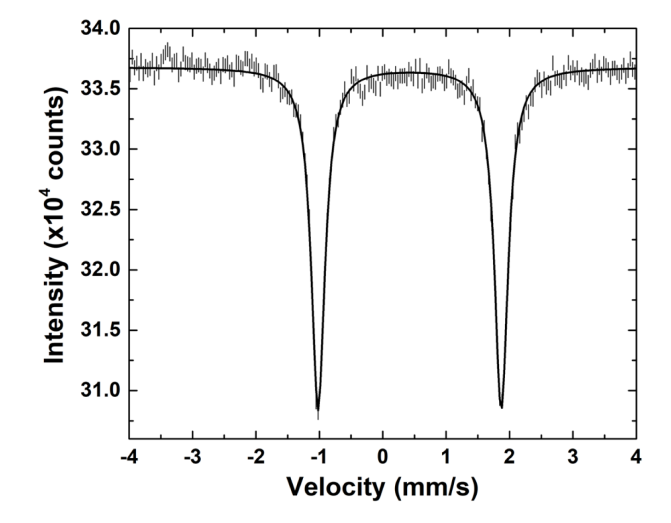


Fig. 4. Mössbauer spectrum of the PcFe(DABCO)₂ complex at 20 K.

Table 1. Selected Mössbauer parameters for PcFeL₂ axially coordinated with ammonia and saturated organic amines.

L	T, K	δ , mm/s	ΔE_Q , mm/s	Reference	
DABCO	20	0.42	2.89	tw	
	293	0.28	2.91	tw	
	293	0.32	2.91	45	
Piperidine	4.2	0.34	2.24	47	
	295	0.28	2.34	47	
$n-C_4H_9NH_2$	77	0.34	1.94	33	
	293	0.25	1.87	45	
NH_3	293	0.26	1.79	48	

atw = this work

PcFe(DABCO)₂ complex and analyzed it using X-ray crystallography. This complex crystallizes in the orthorhombic P₂₁P₂₁P₂ space group with two toluene and one DABCO molecule per PcFe(DABCO)₂. The phthalocyanine core in the target complex is essentially planar and two DABCO ligands are symmetry-related via the inversion center (Fig. 5). As expected from the Mössbauer spectra and simple ligand-field theory considerations, the most sterically hindered DABCO ligands adopt the longest Fe-Naxial bond distances in all reported PcFeL₂ complexes with nitrogen-centered axial ligands (Table 2). One additional DABCO ligand and two toluene solvent molecules were observed in the crystal lattice per phthalocyanine. The free DABCO ligand does not form any hydrogen bonds with available protons in the neighboring molecules. The Fe-N(Pc) bond distances in the PcFe(DABCO)₂ complex are in the typical range for this class of compounds. The experimentally observed elongation of the Fe-N(DABCO) bond distance should lower the energy of the triplet state in the PcFe(DABCO)₂

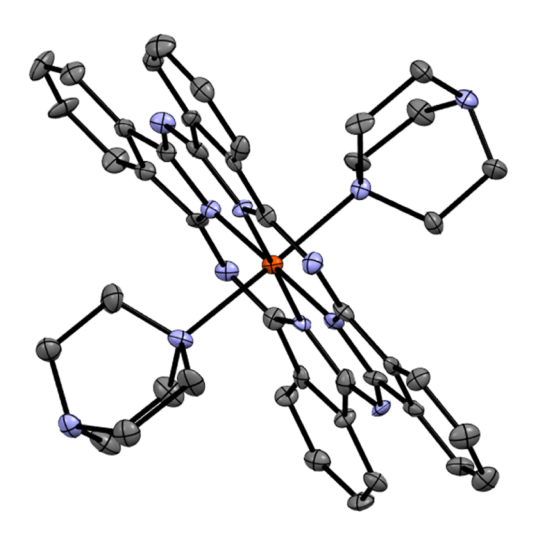


Fig. 5. X-ray structure of the PcFe(DABCO)₂ complex at 50% thermal ellipsoids probability. All hydrogen atoms, two toluene molecules, and a free DABCO ligand are omitted for clarity.

Table 2. Selected X-ray data for PcFeL₂ complexes with ammonia and organic amines.

L	Fe-N(axial) ^a , Å	Fe-N(Pc) ^b , Å	Reference
DABCO	2.227 (2.253)	1.925 (1.943)	tw
4-methylpiperidine	2.119 (2.111)	1.930 (1.946)	36
$PhCH_2NH_2$	2.043	1.920	37
$NHMe_2^{d}$	2.087	1.933	49
$CH_3NH_2^{d}$	2.039	1.932	49
NH_3^{d}	2.017	1.934	49

^aAverage for two axial ligands from X-ray data, DFT-predicted values are in given parentheses; ^baverage for four FeN(Pc) bond distances from X-ray data, DFT-predicted values are in given parentheses; tw = this work; ^docta-substituted Pc^{(a-OEt)8} macrocycle.

complex. Thus, one might expect that the triplet state in this compound can be thermally populated at modestly elevated temperatures. However, the low thermal stability of this compound precluded us from collecting experimental support of this hypothesis.

In agreement with the crystallographic data, the DFT calculations also predict the PcFe(NH₂R)₂ < PcFe(NHR₂)₂ < PcFe(DABCO)₂ trend for the Fe-N_{axial} bond distance in iron phthalocyanines coordinated with aliphatic amines (Table 2). Because of the dramatic increase of the Fe-N(DABCO) bond distance, one might expect that the singlet-triplet energy gap in the PcFe(DABCO)₂ complex should also be small since the PcFe complex has a triplet ground state. Indeed, the DFT calculations confirm this hypothesis and predict a very small (0.23 eV) singlet-triplet energy gap in this compound (Fig. 6). Such a small gap puts a triplet state within the vibrational energy levels of the ground state, making it potentially unstable due to vibronic coupling.

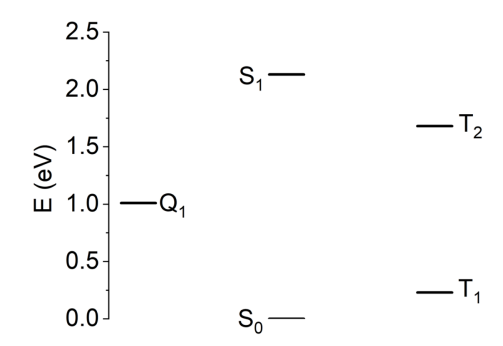


Fig. 6. DFT and TDDFT predicted energy levels of the PcFe(DABCO)₂ complex.

Being curious about the unusual energetics of the PcFe(DABCO), complex, we also calculated the energy of the quintet state, which was found to exist below the Q-band excitation (Fig. 6). The electronic structure of the PcFe(DABCO)₂ complex is typical for this class of compounds with iron-centered d_{xz}, d_{yz}, and d_{xy} MOs being in the HOMO - HOMO-2 region followed by the phthalocyanine-centered a₁₁₁ orbital (in Gouterman's notation for D_{4h} point group, Fig. 7) [50–52]. The Gouterman's a_{2h} occupied MO was predicted to be HOMO-6. The LUMO and LUMO+1 represent Gouterman's pair of eg* MOs followed by the iron-centered d_{22} MO coupled with the nitrogen lone pairs localized on the DABCO ligand. The iron-centered d₂₂ orbital is energetically well-separated from the pair of e_{a*} MOs, but because of the long Fe-N(DABCO) bond distance, it has low energy compared to the iron-centered d_{z2} orbital in PcFeL₂ complexes with primary and secondary alkylamines as the axial ligands. Similar to our previous observations [43], the phthalocyanine-centered b_{1u*} and b_{2u*} MOs were predicted to be only ~0.1 eV apart implying a small separation between

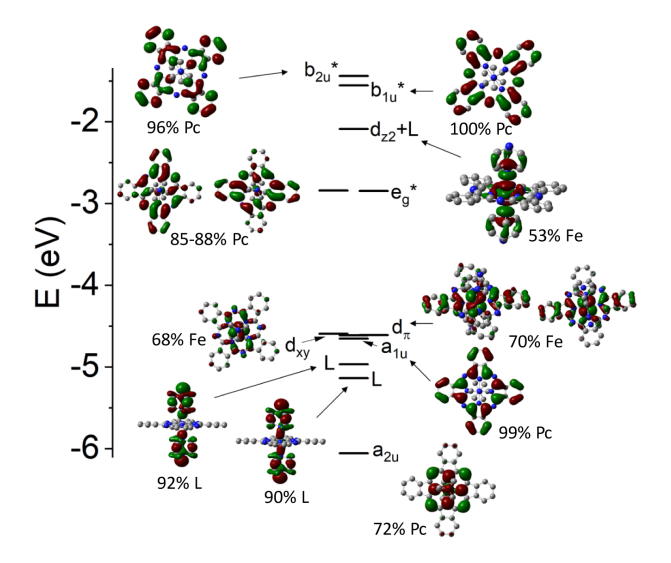


Fig. 7. DFT-predicted energy diagram and images of the frontier MOs in the PcFe(DABCO)₂ complex.

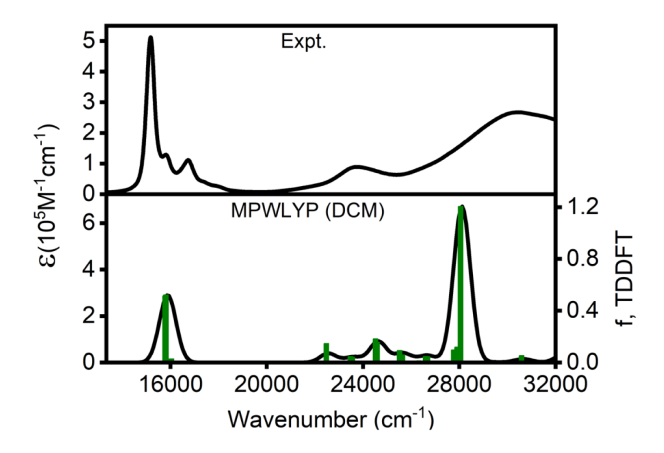


Fig. 8. TDDFT-predicted and experimental spectra of the PcFe(DABCO)₂ complex in an energy scale.

the MLCT₁ and MLCT₂ bands in the UV-Vis and MCD spectra of this compound (Fig. 7).

The TDDFT-predicted UV-Vis spectrum of the $PcFe(DABCO)_2$ complex is shown in Fig. 8. The predicted Q-band position at 633 nm correlates well with the experimental observations. In agreement with the previous work, this doubly degenerate transition is dominated by the $a_{1u} \rightarrow e_{g^*}$ single-electron excitation and is phthalocyanine-centered. Another doubly degenerate transition predicted at 624 nm (excited states 10 and 11, Table 3) has ILCT character and is dominated by the DABCO $\rightarrow e_{g^*}$ single-electron excitations. The low energy of this transition is reflective of the weak coordination of the DABCO ligands (which do not stabilize the lone-pair dominated HOMO-4 and HOMO-5 centered on DABCO much) and long Fe-N(DABCO) bond distance. The MLCT₁

Table 3. Selected TDDFT-predicted excited states in PcFe(DABCO)₂ and the [(DABCO)PcFe]₂(DABCO) dimer.

ES	E, cm ⁻¹	λ, nm	f	Assignment/composition	
PcFe(DABCO) ₂					
8	15777	634	0.515	<i>Q</i> -band 91.0% H-3 \rightarrow LUMO	
9	15812	632	0.523	<i>Q</i> -band 91.5% H-3 \rightarrow L+1	
19	23480	426	0.046	$\begin{array}{c} \text{MLCT}_1 \text{ 44.2\% HOMO} \rightarrow \text{L+3}, \\ \text{43.8\% H-1} \rightarrow \text{L+3} \end{array}$	
20	23562	424	0.040	MLCT ₁ 79.1% H-2 \rightarrow L+3, 15.4% H-1 \rightarrow L+3	
23	24519	408	0.183	$\begin{array}{c} \text{MLCT}_2 \ 53.1\% \ \text{HOMO} \rightarrow \text{L+4}, \\ 31.7\% \ \text{H-1} \rightarrow \text{L+4} \end{array}$	
24	24585	407	0.156	MLCT ₂ 75.0% H-2 \rightarrow L+4, 14.9% H-1 \rightarrow L+4	
[(DABCO)PcFe] ₂ (DABCO)					
33	15843	631	1.016	<i>Q</i> -band 38.6% H-7 → L+1, 32.7% H-6 → LUMO	
34	15867	630	1.017	<i>Q</i> -band 43.6% H-6 → L+3, 41.0% H-7 → L+2	

and MLCT₂ bands were predicted in the 407-430 nm range and are, similar to the other PcFeL2 complexes, separated by ~ 0.1 eV. We also optimized the geometry and calculated the UV-Vis spectrum of the (DABCO) PcFe(DABCO)PcFe(DABCO) dimer in which the central DABCO ligand is coordinated to both of the iron phthalocyanines. The optimized geometry for the dimer has bond distances close to the monomer Fe-N(DABCO) bond (2.253 Å for the monomer and 2.244 Å in the dimer). Separated by a bridging DABCO molecule, two phthalocyanine ligands form an H-type aggregate with an interplanar distance of 7.159 Å. This is a much larger interplanar distance compared to the traditional (PcM)₂O or Pc_2M systems (3.0 – 3.55 Å) [53, 54]. Such a large interplanar distance should significantly reduce the excitonic coupling between the two phthalocyanine ligands as the magnitude of this excitonic coupling is inversely proportional to the cube of the inter-chromophoric distance. Not surprisingly, TDDFT calculations predict only a \sim 1 nm blue-shift between the Q-band in the monomeric PcFe(DABCO)₂ and dimeric (DABCO)PcFe(DABCO) PcFe(DABCO) complexes (Table 3). Thus, the new band in the UV-Vis spectrum of the PcFe(DABCO), complex observed at 627 nm upon initial heating or prolonged laser irradiation of the sample (Fig. 9) cannot be attributed to the formation of a (DABCO)[PcFe(DABCO)]_n polymer, which is expected to have a Q-band close in energy to the monomer. However, this 627 nm band can be attributed to the formation of a [(DABCO)PcFe]₂O complex since (LPcFe)2O systems (L is organic amine or N-heterocycle) possess a O-band located between 615 and 630 nm [54]. Thus, the temperature-stimulated degradation of the PcFe(DABCO), complex can be summarized as shown in Fig. 9 and Scheme 1.

The excited state dynamics of the PcFe(DABCO)₂ complex were investigated by time-resolved spectroscopy. During the transient absorption experiments, we observed partial degradation of the sample during the time required to acquire multiple scans. Figure 9a presents the absorption spectrum of the sample prior to the pump-probe experiments and 1.5 hours after the last scan, a total of 8 hours after starting the experiment. The change in the spectrum is consistent with the formation of the [(DABCO)PcFe]₂O ($\lambda_{max} = 627 \text{ nm}$) and (PcFe)₂O $(\lambda_{\text{max}} = 690 \text{ nm})$ complexes [46, 54]. In order to assess the impact of sample degradation during the pump-probe experiments, Fig. 9b presents a comparison of the first, second, and eighth scans at two different pump-probe delay times. There was very little change between the first and second scans; however, by scan 8, the difference became apparent including an additional GSB around 625 nm and a reduction in the TA around 700 nm. The impact of the sample transformation was not as significant in the pump-probe measurements as it was in the absorption measurements, and this may reflect the preferential excitation of the monomers at 400 nm. In order

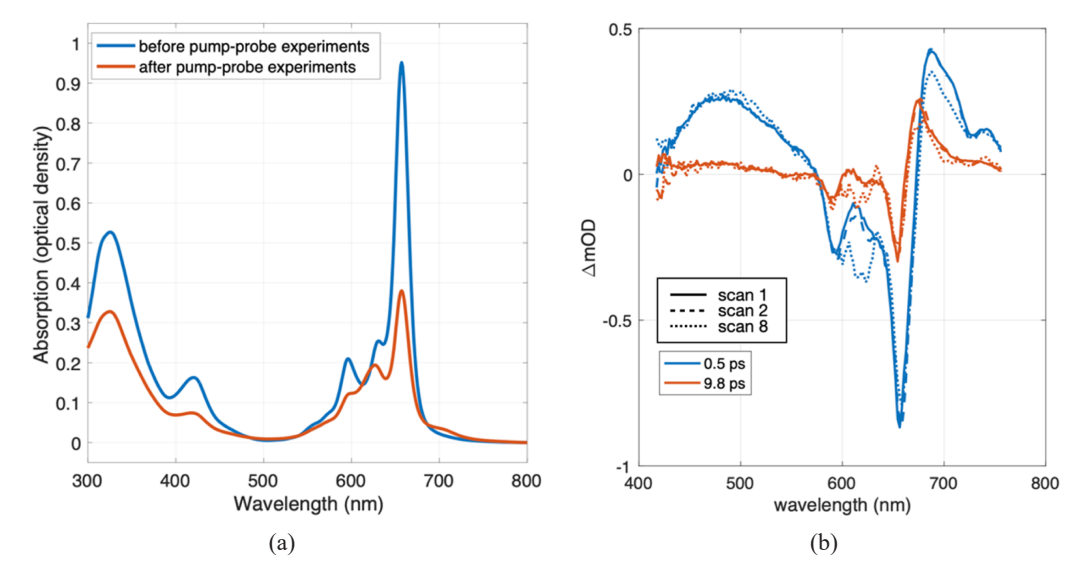


Fig. 9. (a) The absorption spectrum of the pump-probe sample prior to the pump-probe experiments and 1.5 hours after the pump-probe experiments. (b) A comparison of the pump-probe scans at two delay times. The first two scans are nearly indistinguishable; however, by scan 8 there is a deviation in the difference spectrum as a result of dimerization.

to minimize the impact of the dimerization, only the first scan was used in the data analysis.

The first scan from the pump-probe data is presented in Figs. 10a and 10c. At the earliest delay times and within the instrument response, there is transient absorption (TA) at shorter (450–550 nm) and longer (>675 nm) wavelengths, and a ground state bleach (GSB) that mirrors the absorption spectrum at wavelengths in between 575–675 nm. We assign these features to the initial excited state. The TA at shorter wavelengths decays very rapidly and this is accompanied by an increase in TA at longer wavelengths that subsequently shifts to shorter wavelengths and then decays together with the GSB.

In order to characterize the time scales and associated changes in the transient spectra, the data were fitted using a set of three basis difference spectra taken from the original data set at delay times of 0, 0.5, and 10 ps and are presented in Fig. 10e. The full data set was modeled as the sequential first-order evolution from one different spectrum to the next.

$$a(t)w_A A(\lambda) \xrightarrow{k_1} b(t)w_B B(\lambda) \xrightarrow{k_2} c(t)w_C C(\lambda) \xrightarrow{k_3} d(t)D(\lambda).$$
 (1)

In Eq. (1), the capital letters, A-D, represents the normalized basis difference spectra presented in Fig. 10e. The D(λ) difference spectrum was set to zero at all wavelengths as the final outcome. The time-dependent coefficients, a(t)-d(t), were always restricted to sum to 1, and the appropriate differential equation was solved with the initial condition set to a(t=0)=1. The individual weights, w_A-w_C , and the first-order rate coefficients, k_1 - k_3 , were optimized to minimize the residual between the simulated data and the raw data at all delay times between 0 and 1 ns and all wavelengths between 460 and 750 nm.

Figures 10b and 10d presents the optimized fit to the pump-probe data using Eq. (1) and the optimized fitting parameters presented in Table 4. Figure 10f presents the time evolution of the weights (the product of the time-dependent coefficient and w_x) for the basis difference spectra in Fig. 10e. Comparing Figs. 10a and 10d, the data is well represented by the sequential evolution between the three difference spectra in Fig. 10e. The difference spectrum A in Fig. 10e represents the initially exited state. The rapid loss of the TA at shorter wavelengths and correlated increase in TA on the long wavelength side of the GSB tracks the loss of the initially excited state in 220 fs.

The differential shape of the GSB that evolves following the deactivation of the initially excited state is consistent with a vibrationally hot ground state. The hot ground state absorbs at longer wavelengths. As the ground state cools, the hot absorption shifts to shorter wavelengths, and this shift were evident in the transition from difference spectrum B to C in Fig. 10e. The cooling ground state eventually recovers to thermal equilibrium resulting in the loss of the difference spectrum (difference spectrum D). Although the ground state cooling was well modeled by a sequential set of first-order events with time constants of 2.6 ps and 26.8 ps, this should not be interpreted as two separable steps. Cooling in the ground state will have a time-dependent rate coefficient. The rate slows with time as the vibrations cool. This behavior was captured well enough with the two-time constants that are an order of magnitude apart, but this does not mean there are separable steps with independent time

Our overall interpretation of the measurements is that the initially excited state rapidly converts to the ground state in 220 fs, and the vibrationally hot ground state relaxes on time scales that slow from 2.6 ps to 26.8 ps.

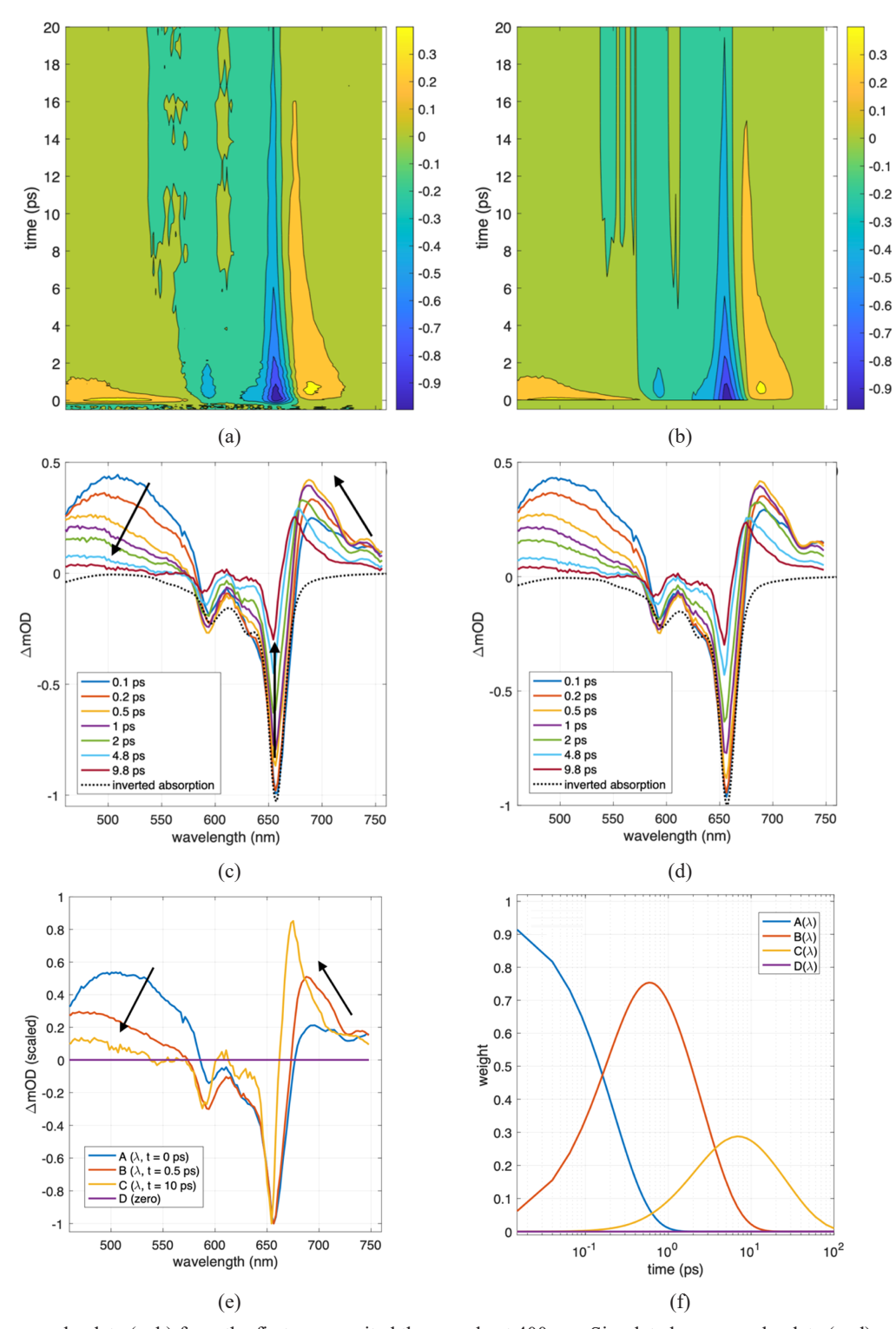


Fig. 10. Pump-probe data (a, b) from the first scan excited the sample at 400 nm. Simulated pump-probe data (c, d) using the basis difference spectra presented in (e), Eq. (1), and the optimized parameters presented in Table 4. Time evolution (f) of the weights for the individual basis difference spectra in (e) as determined by Eq. (1).

Table 4. The optimized fitting parameters in Eq. (1). The resulting fit is presented in Fig. 10.

$1/k_1$	$1/k_2$	$1/k_{3}$	w_{A}	w_{B}	$w_{\rm C}$
220 fs	2.6 ps	26.8 ps	0.98	0.95	0.37

The excited state dynamics are short-lived, with a return to the thermally equilibrated ground state in less than 50 ps. It is possible that the low-lying triplet state is involved in the rapid deactivation of the initial excited state, however, there is no direct evidence for an additional state in the transient difference spectra.

EXPERIMENTAL

Synthesis of PcFe (DABCO),

Initially, the reaction was carried out in a Schlenk tube under an argon atmosphere where 10 equivalents of solid DABCO were added to 250 mg of iron(II) phthalocyanine and heated. The DABCO melted and was used as the solvent for the reaction; however, due to its willingness to readily sublime, the DABCO would crystallize on the upper portion of the reaction tube and had to be pushed back down several times with difficulty. In the end, a microwave procedure was found to be more effective.

Therefore, 500 mg (0.88 mmol) of iron(II) phthalocyanine (Sigma-Aldrich) and 3.5 g (31.20 mmol) of DABCO were added to a glass microwave reaction tube, sealed, and purged with nitrogen. The tube was vigorously shaken before placing it in the microwave reactor to ensure that the materials were thoroughly mixed together. The following microwave parameters were utilized: t = 15 mins, T = 170 °C, and P = 400W. The whitish-green product can be purified via sublimation at room temperature for eight hours or until dark green; however, the product appears to degrade/polymerize once the excess DABCO ligand is completely removed or if the product is heated. ¹H NMR (500 MHz, ppm): 9.72 (q 8H, AA'BB', α -Pc), 7.85 (q 8H, AA'BB', β -Pc), 2.09 (s 12H) DABCO), 1.60 (s 12H, DABCO). Elemental analysis: Calc. for PcFe(DABCO)₂ × H_2O × 0.5DABCO: C 65.12 H 5.58, N 21.01; Found: C 65.02, H 5.30, N 21.37.

UV-Vis/MCD spectroscopy

All UV-vis spectra were collected on a Jasco V-770 spectrophotometer and MCD spectra were measured with a Jasco J-1500 CD spectrometer using a permanent 1.4 T magnet. The MCD spectra were recorded in mdeg = $[\theta]$ and converted to molar ellipticity as $\Delta \varepsilon = \theta/(32980 \times \text{Blc})$; where B is the magnetic field, l is the path length (in cm), and c is the concentration (in M).⁵⁵ The completed MCD spectra were measured in parallel and antiparallel orientations with respect to the magnetic field.

Mössbauer spectra

Mössbauer spectra were collected either at 20 K or room temperature. Mössbauer spectroscopy experiments were performed in zero fields in transmission geometry with a 10 GBq [57] Co-in-Rh source and WissEl constant acceleration drive. Low-temperature spectra were collected using a Janis SHI-850 closed-cycle refrigerator. All spectra were calibrated relative to α-Fe or sodium nitroprusside at room temperature. A non-linear least squares analysis was applied to the Mössbauer spectra for fitting. Each Fe-site was characterized by a Lorentzian lineshape doublet and an isomer shift whose energies were set by the appropriate nuclear transitions.

In-house produced codes or Mossfit software were used for the data analyses.

Computational aspects

All calculations were run using Gaussian 16 [56]. TPSSh [57, 58] with Wachter's full-electron basis set [59] (Wf) for iron and the 6-311G(d) basis set [60] for the other atoms were used for all geometry optimizations. Vibrational frequencies were calculated to ensure all geometries were local minima. Time-dependent density functional theory (TDDFT) with MPWLYP [61] was used to calculate the first 80 excited states for the monomer and 50 excited states for the dimer. The same basis sets as for the geometry optimizations were used for the TDDFT calculations. Single-point calculations using the same parameters as the TDDFT calculations were also performed. All calculations were run in solution using the PCM model [62], with DCM as the solvent. QMForge [63] was used to process the TDDFT data.

X-Ray crystallography

The crystalline samples were mounted on a 150 mm MiTeGen Dual-Thickness MicroMount using *n*-paratone oil (Hampton) and data were collected at 150 K. The diffraction data were collected using a Bruker SMART APEX-II Single-Crystal diffractometer with a TRI-UMPH mono-chromated Mo K α radiation (λ =0.71073 A) source with a crystal-to-detector distance of 50 mm, using a series of θ and ω scans in 0.50° oscillations. The data was processed and corrected for Lorentz and polarization effects and an empirical absorption correction was applied, using the Bruker Apex II software suite [64]. The structures were solved with SIR92 [65, 66], and subsequent refinements were performed using the Crystals for Windows crystallographic software package [67]. The coordinates and anisotropic displacement parameters for the non-hydrogen atoms were refined. Hydrogen atoms were placed in idealized geometric positions and linked to their respective carbon atoms using a riding model during refinement. The disordered DABCO molecule was eliminated with the PLATON SQUEEZE [68] procedure. Complete structural data on PcFe(DABCO)₂ complex can be accessed using CCDC reference number 2232624.

Time-resolved photophysics

Transient absorption measurements were performed using a Ti: Sapphire-based home-built laser system that produces 1 mJ pulses centered at 800 nm at 1 kHz. The majority of the output was frequency doubled to 400 nm using a 2 mm thick BBO crystal to create the excitation (pump) pulses, and a small fraction of the output was split off and focused into a 2 mm thick sapphire plate to generate a continuum probe spanning 450–780 nm. The pump and probe pulses were focused and crossed in the sample cell, a 2 mm path-length quartz cuvette. At the crossing

point, the pump had a waist of 245 μ m (1/e₂) and the probe had a waist of 150 µm (1/e₂). The pump intensity was attenuated to 30 μJ/pulse before the sample. The timing between the pump and probe pulses was controlled using retroreflectors mounted on mechanical delay stages (Newport UTM150PP.1). The pump and probe were both linearly polarized, and their polarization was set at 54.7 degrees apart to minimize anisotropic dynamics in the measurements. The instrument response was 80 fs (Gaussian, FWHM). After the sample, the continuum probe was collimated and refocused into a monochromator (Princeton Instruments SP2150i monochromator 150 lines/ mm, 500 nm blaze) and dispersed onto a linear 256-pixel silicon diode array (Hamamatsu S3902-256Q) resulting in wavelength resolution of 2 nm per pixel. The pulse spectrum was measured for every individual laser shot. The pump pulse was modulated at half the laser repetition rate, and the change in optical density was determined for every consecutive pair of probe pulses (pump on minus pump off). The signals were averaged for 10,000 laser pulse pairs at each delay time, and the full set of the time delays was stepped over to accumulate a single scan. This was then repeated for 8 scans. The data were corrected for the temporal chirp in the continuum probe pulse. The sample was dissolved in dichloromethane and had an optical density of 0.12 at the pump wavelength of 400 nm in the 2 mm path length sample cell. The sample was purged with nitrogen immediately prior to the measurements, and the sealed sample cell was continuously translated during the experiments to slow the rate of sample degradation.

CONCLUSIONS

The PcFe(DABCO)₂ complex was prepared under microwave irradiation conditions and was found to be unstable under heat or in the absence of excess DABCO ligand. Under heat or laser radiation, it rapidly converts into the (PcFe)₂O μ-oxo dimer, even at a modest temperature. The target molecule was characterized by UV-Vis, MCD, ¹H NMR, and Mössbauer spectroscopies. The X-ray crystal structure of this complex is indicative of the longest Fe-N(DABCO) bond distance among all known PcFeL₂ complexes with nitrogen donors as the axial ligands. The electronic structure of the PcFe(DABCO)₂ complex was elucidated by DFT and TDDFT methods. The DFT calculations predicted a very small singlettriplet gap in this compound. The femtosecond transient absorption spectroscopy is indicative of extremely fast (~200 fs) deactivation of the first excited state in PcFe(DABCO)₂ and the lack of the formation of the long-lived low-energy triplet state.

Acknowledgments

Generous support from the NSF (CHE-2153081), Minnesota Supercomputing Institute, and the University of Tennessee to VN is greatly appreciated.

Supporting information

Crystallographic data have been deposited at the Cambridge Crystallographic Data Centre (CCDC) under the numbers CCDC-2232624. Copies can be obtained on request, free of charge, *via* https://www.ccdc.cam.ac.uk/structures/ or from the Cambridge Crystallographic Data Centre, 12 Union Road, Cambridge CB2 1EZ, UK (fax: +44 1223-336-033 or email: deposit@ccdc.cam.ac.uk)

REFERENCES

- 1. Ercolani C, Jubb J, Pennesi G, Russo U and Trigiante G. *Inorg. Chem.* 1995; **34**: 2535–2541.
- 2. Ercolani C, Gardini M, Goedken VL, Pennesi G, Rossi G, Russo U and Zanonato P. *Inorg. Chem.* 1989; **28**: 3097–3099.
- 3. Kennedy, BJ, Murray KS, Zwack PR, Homborg H and Kalz W. *Inorg. Chem.* 1986; **25**: 2539–2545.
- 4. Nemykin VN, Chernii VYa, Volkov SV, Bundina NI, Kaliya OL, Li VD and Lukyanets EA. *J. Porphyrins Phthalocyanines* 1999; **3**: 87–98.
- Nemykin VN, Purchel AA, Spaeth AD and Barybin MV. *Inorg. Chem.* 2013; 52: 11004–11012.
- 6. Silver J, Lukes P, Houlton A, Howe S, Hey P and Ahmet MT. *J. Mater. Chem.* 1992; **2**: 849–855.
- Afanasiev P and Sorokin AB. Acc. Chem. Res. 2016; 49: 583–593.
- 8. Sorokin AB, Chem. Rev. 2013; 113: 8152-8191.
- Woehrle D, Suvorova O, Gerdes R, Bartels O, Lapok L, Baziakina N, Makarov S and Slodek A. J. Porphyrins Phthalocyanines 2004; 8: 1020–1041.
- 10. Zagal JH, Coord. Chem. Rev. 1992; 119: 89–136.
- Kudrik EV and Sorokin AB. J. Mol. Catal. A: Chemical, 2017; 426: 499–505.
- Geraskin IM, Pavlova O, Neu HM, Yusubov MS, Nemykin VN and Zhdankin VV. Adv. Synth. Catal. 2009; 351: 733–737.
- 13. Neu HM, Zhdankin VV and Nemykin VN. *Tetr. Lett.* 2010; **51**: 6545–6548.
- 14. Griffin JR, Wendell CI, Garwin JA and White MC. J. Am. Chem. Soc. 2017; **139**: 13624–13627.
- He C, Wu Z-Y, Zhao L, Ming M, Zhang Y, Yi Y and Hu J-S. ACS Catalysis 2019; 9: 7311–7317.
- Kozack CV, Sowin JA, Jaworski JN, Iosub AV and Stahl SS. ChemSusChem 2019; 12: 3003–3007.
- 17. Hu P, Tan M, Cheng L, Zhao H, Feng R, Gu W-J and Han W. *Nature Commun*. 2019; **10**: 1–9.
- Neu HM, Yusubov MS, Zhdankin VV and Nemykin VN. *Adv. Synth. Catal.* 2009; **351**: 3168–3174.
- Fitzgerald JP, Lebenson JR, Wang G, Yee GT, Noll BC and Sommer RD. *Inorg. Chem.* 2008; 47: 4520–4530.
- Fitzgerald JP, Haggerty BS, Rheingold AL, May L and Brewer GA. *Inorg. Chem.* 1992; 31: 2006–2013.

- Ona-Burgos P, Casimiro M, Fernandez I, Navarro AV, Fernandez-Sanchez JF, Carretero AS and Gutierrez AF. *Dalton Trans.* 2010; 39: 6231–6238.
- Valero-Navarro A, Fernandez-Sanchez JF, Segura-Carretero A, Spichiger-Keller UE, Fernandez-Gutierrez A, Ona P and Fernandez I. J. Porphyrins Phthalocyanines 2009; 13: 616–623.
- 23. Fernandez-Sanchez JF, Fernandez I, Steiger R, Beer R, Cannas R and Spichiger-Keller UE. *Adv. Functional Mater.* 2007; **17**: 1188–1198.
- Govan J, Abarca G, Aliaga C, Sanhueza B, Orellana W, Cardenas-Jiron G, Zagal JH and Tasca F. *Electrochem. Commun.* 2020; 118: 106784.
- Praats R, Kaarik M, Kikas A, Kisand V, Aruvali J, Paiste P, Merisalu M, Leis J, Sammelselg V and Zagal JH. *Electrochim. Acta* 2020; 334, 135575.
- Recio FJ, Gutierrez CA, Venegas R, Linares-Flores C, Caro CA and Zagal JH. *Electrochim. Acta* 2014; 140: 482–488.
- 27. Hanack M, Knecht S, Polley R and Subramanian LR. *Synth. Metals* 1996; **80**: 183–189.
- 28. Watkins JJ and Balch AL. *Inorg. Chem.* 1975; **14**: 2720–2723.
- Calderazzo F, Frediani S, James BR, Pampaloni G, Reimer KJ, Sams JR, Serra AM and Vitali D. *Inorg. Chem.* 1982; 21: 2302–2306.
- Nemykin VN, Nevonen DE, Osterloh WR, Ferch LS, Harrison LA, Marx BS and Kadish KM. *Inorg. Chem.* 2021; 60: 16626–16644.
- Nemykin VN, Nevonen DE, Ferch LS, Shepit M, Herbert DE and van Lierop J. *Inorg. Chem.* 2021;
 60: 3690–3706.
- 32. Jones JG and Twigg MV. *J. Chem. Soc. Dalton Trans.* 1978; 1709–1714.
- 33. Dale BW, Williams RJP, Edwards PR and Johnson CE. *Trans. Faraday Soc.* 1968; **64**: 620–629.
- 34. Dale BW, Williams RJP, Edwards PR and Johnson CE. *Trans. Faraday Soc.* 1968; **64**: 3011–3013.
- 35. Dale BW, Trans. Faraday Soc. 1969; **65**: 331–339.
- Nemykin VN, Kobayashi N, Chernii VY and Belsky VK. Eur. J. Inorg. Chem. 2001; 2001: 733–743. DOI: 10.1002/1099–0682(200103)2001:3<733::AID-EJIC733>3.0.CO;2–2.
- 37. Fernandez I, Pregosin PS, Albinati A, Rizzato S, Spichiger-Keller UE, Nezel T and Fernandez-Sanchez JF. *Helvetica Chim. Acta* 2006; **89**: 1485–1496.
- Nevonen DE, Ferch LS, Chernii VY, Herbert DE, van Lierop J and Nemykin VN. J. Porphyrins Phthalocyanines 2020; 24: 894–903.
- 39. Ettorre R, Marton D, Russo U and Zanonato P. *J. Porphyrins Phthalocyanines* 2001; **5**: 545–547.
- Ouedraogo GV, More C, Richard Y and Benlian D. *Inorg. Chem.* 1981; 20: 4387–4393.
- 41. Ough EA and Stillman MJ. *Inorg. Chem.* 1994; **33**: 573–583.
- 42. Stillman MJ and Thomson AJ. *J. Chem. Soc. Fara-day Trans.* 2, 1974; **70**: 805–814.

- 43. Nevonen DE, Ferch LS, Schrage BR and Nemykin VN. *Inorg. Chem.* 2022; **61**: 8250–8266.
- 44. Schneider O and Hanack M. Chem. Ber. 1983; **116**: 2088–2108.
- Hanack M, Keppeler U, Lange A, Hirch A and Dieing R. in: Phthalocyanines: Properties and Applications, Leznoff CC, Lever ABP (Eds.) VCH 1993;
 Vol 2: 43–96
- Nemykin VN, Chernii VYa, Volkov SV, Bundina NI, Kaliya OL, Li VD and Lukyanets EA. J. Porphyrins Phthalocyanines 1999; 3: 87–98.
- 47. James BR, Sams JR, Tsin TB and Reimer KJ. *J. Chem. Soc. Chem. Commun.* 1978; 746–747.
- 48. Hanack M and Hirsch A. Synth. Met. 1989; 29: F9.
- Wang Z, Johnson SI, Wu G and Ménard G. *Inorg. Chem.* 2021; 60: 8242–8251.
- 50. Zerner M and Gouterman M. *Theor. Chim. Acta* 1966; **4**: 44–63.
- 51. Zerner M and Gouterman M. *Inorg. Chem.* 1966; **5**: 1699–1706.
- Zerner M and Gouterman M. *Theor. Chim. Acta* 1967; 8: 26–34.
- 53. Wynne KJ, *Inorg. Chem.* 1985; **24**: 1339–1342.
- Ercolani C, Monacelli F, Dzugan S, Goedken VL, Pennesi G and Rossi G. J. Chem. Soc. Dalton Trans. 1991; 1309–1315.
- 55. Galinato MGI, Spolitak T, Ballou DP and Lehnert N. *Biochemistry* 2011; **50**: 1053–1069.
- 56. Gaussian 16, Revision B.01, Frisch MJ, Trucks DW, Schlegel HB, Scuseria GE, Robb MA, Cheeseman JR, Scalmani G, Barone V, Petersson GA, Nakatsuji H, Li X, Caricato M, Marenich A, Bloino J, Janesko BG, Gomperts R, Mennucci B, Hratchian HP, Ortiz JV, Izmaylov AF, Sonnenberg JL, Williams-Young D, Ding F, Lipparini F, Egidi F, Goings J, Peng B, Petrone A, Henderson T, Ranasinghe D, Zakrzewski VG, Gao J, Rega N, Zheng G, LiangW, Hada M, Ehara M, Toyota K, Fukuda R, Hasegawa J, Ishida M, Nakajima T, Honda Y, Kitao O, Nakai H, Vreven T, Throssell K, Montgomery Jr. JA, Peralta JE, Ogliaro F, Bearpark M, Heyd JJ, Brothers E, Kudin KN, Staroverov VN, Keith T, Kobayashi R, Normand J, Raghavachari K, Rendell A, Burant JC, Iyengar SS, Tomasi J, Cossi M, Millam JM, Klene M, Adamo C, Cammi R, Ochterski JW, Martin RL, Morokuma K, Farkas O, Foresman JB and Fox DJ. Gaussian, Inc. Wallingford CT, 2016.
- 57. Tao JM, Perdew JP, Staroverov VN and Scuseria GE. *Phys. Rev. Lett.* 2003; **91**: 146401/1–146401/4.
- 58. Staroverov VN, Scuseria GN, Tao J and Perdew JP. *J. Chem. Phys.* 2003; **119**: 12129–12137.
- 59. Wachters AJH, *J. Chem. Phys.* 1970; **52**: 1033–1036.
- McLean AD and Chandler GS. J. Chem. Phys. 1980; 72: 5639–5648.
- 61. Schultz NE, Zhao Y and Truhlar DG. *J. Phys. Chem. A.* 2005; **109**: 11127–11143.

- 62. Tomasi J, Mennucci B and Cammi R. Chem. Rev. 2005; **105**: 2999-3093.
- 63. Tenderholt AL, QMForge, version 2.1; Standord University: Stanford, CA, 2011. https://gmforge. net/.
- 64. SAINT, version 7.46A; Bruker Analytical X-ray System: Madison, WI, 1997-2007.7 SADABS. Bruker Nonius area detector scaling and absorption correction, V2.10; Bruker AXS Inc.: Madison, WI, 2003.
- 65. Altomare A, Burla MC, Cammalli G, Cascarano M, Giacovazzo C, Guagliardi A, Moliterni AGG, Polidori G and Spagna A. J. Appl. Crystallogr. 1999; 32: 115-119.
- 66. Altomare A, Cascarano G, Giacovazzo C and Guagliardi A. J. Appl. Crystallogr. 1993; 26: 343-350.
- 67. Betteridge PW, Carruthers JR, Cooper RI, Prout K and Watkin DJ. J. Appl. Cryst. 2003; 36: 1487.
- 68. SHELXTL, Version 5.1; Bruker AXS Inc.: Madison, WI, 1997.